SLAC-PUB-14542

Fermi Large Area Telescope Observations of the Cygnus Loop Supernova Remnant

H. Katagiri[1,2], L. Tibaldo[3,4,5,6,7], J. Ballet[5], F. Giordano[8,9], I. A. Grenier[5], T. A. Porter[10], M. Roth[11], O. Tibolla[12], Y. Uchiyama[10], R. Yamazaki[13]

Received ________________; accepted ________________

[1]College of Science, Ibaraki University, 2-1-1 Bunkyo, Mito, Ibaraki 310-8512, Japan

[2]email: katagiri@mx.ibaraki.ac.jp

[3]Istituto Nazionale di Fisica Nucleare, Sezione di Padova, I-35131 Padova, Italy

[4]Dipartimento di Fisica "G. Galilei", Università di Padova, I-35131 Padova, Italy

[5]Laboratoire AIM, CEA-IRFU/CNRS/Université Paris Diderot, Service d'Astrophysique, CEA Saclay, 91191 Gif sur Yvette, France

[6]Partially supported by the International Doctorate on Astroparticle Physics (IDAPP) program

[7]email: luigi.tibaldo@pd.infn.it

[8]Dipartimento di Fisica "M. Merlin" dell'Università e del Politecnico di Bari, I-70126 Bari, Italy

[9]Istituto Nazionale di Fisica Nucleare, Sezione di Bari, 70126 Bari, Italy

[10]W. W. Hansen Experimental Physics Laboratory, Kavli Institute for Particle Astrophysics and Cosmology, Department of Physics and SLAC National Accelerator Laboratory, Stanford University, Stanford, CA 94305, USA

[11]Department of Physics, University of Washington, Seattle, WA 98195-1560, USA

[12]Institut für Theoretische Physik and Astrophysik, Universität Würzburg, D-97074 Würzburg, Germany

[13]Department of Physics and Mathematics, Aoyama Gakuin University, Sagamihara, Kanagawa, 252-5258, Japan

Work supported in part by US Department of Energy contract DE-AC02-76SF00515.

SLAC National Accelerator Laboratory, Menlo Park, CA 94025

To be submitted to ApJ: v6.8, August 11, 2011

ABSTRACT

We present an analysis of the gamma-ray measurements by the Large Area Telescope (LAT) onboard the *Fermi Gamma-ray Space Telescope* in the region of the supernova remnant (SNR) Cygnus Loop (G74.0−8.5). We detect significant gamma-ray emission associated with the SNR in the energy band 0.2–100 GeV. The gamma-ray spectrum shows a break in the range 2–3 GeV. The gamma-ray luminosity is $\sim 1 \times 10^{33}$erg s^{-1} between 1–100 GeV, much lower than those of other GeV-emitting SNRs. The morphology is best represented by a ring shape, with inner/outer radii $0^\circ.7 \pm 0^\circ.1$ and $1^\circ.6 \pm 0^\circ.1$. Given the association among X-ray rims, Hα filaments and gamma-ray emission, we argue that gamma rays originate in interactions between particles accelerated in the SNR and interstellar gas or radiation fields adjacent to the shock regions. The decay of neutral pions produced in nucleon-nucleon interactions between accelerated hadrons and interstellar gas provides a reasonable explanation for the gamma-ray spectrum.

Subject headings: cosmic rays — acceleration of particles — ISM: individual objects (the Cygnus Loop) — ISM: supernova remnants — gamma rays: ISM

1. Introduction

Diffusive acceleration by supernova shock waves can accelerate particles to very high energies (e.g., Blandford & Eichler 1987). Gamma-ray observations are a useful probe of these mechanisms complementary to other wavebands. So far, observations by the Large Area Telescope (LAT) on board the *Fermi Gamma-ray Space Telescope* have demonstrated that bright gamma-ray sources coincident with middle-aged supernova remnants (SNRs) interacting with dense molecular clouds (Abdo et al. 2009, 2010a,b,e,f) exhibit steep gamma-ray spectra above a few GeV. A possible conventional explanation for these spectral properties is that the energy distribution of cosmic rays (CR) is greatly influenced by their diffusive transport (e.g., Aharonian & Atoyan 1996; Gabici et al. 2009; Torres et al. 2010; Ohira et al. 2011). On the other hand, these features can also be explained by reacceleration of pre-existing cosmic rays at a cloud shock and subsequent adiabatic compression where strong ion-neutral collisions accompanying Alfv́en wave evanescence lead to a steepening of the spectrum of accelerated particles (Uchiyama et al. 2010). Furthermore, using three-dimensional magnetohydrodynamic simulations, Inoue et al. (2010) show that the interaction between a supernova blast wave and inhomogeneous interstellar clouds formed by thermal instability generates multiple reflected shocks, which can further energize cosmic-ray particles originally accelerated at the blast-wave shock and produce the spectral break. Since the gamma-ray bright regions are expected to be different in the aforementioned models, studying SNRs with large apparent sizes can help to disentangle the origin of the spectral features.

The Cygnus Loop (G74.0−8.5) is one of the most famous and well-studied middle-aged SNRs. The size ($\sim 3^\circ$) makes it an ideal candidate for detailed morphological studies in high-energy gamma rays since it is larger than the LAT angular resolution above a few hundred MeV. The large angular offset from the Galactic plane ($b \sim -8^\circ.5$) reduces the problems of background contamination and permits a detailed study of the environment around the shock region by means of infrared/optical/UV observations. The shell-like X-ray emission from thermal plasma is prominent in the northern region of the remnant, with a blowout in the southern rim (Ku et al. 1984). The radio spectrum from the limb-brightened shells is non-thermal (Keen et al. 1973). No correlation with dense molecular clouds has been reported, although blast waves on the western limb might encounter molecular material (Scoville et al. 1977). The distance from the Earth is estimated to be 540^{+100}_{-80} pc based on the proper motion of optical filaments in conjunction with models of non-radiative shocks (Blair et al. 2005). The age has been estimated to be $\sim 2 \times 10^4$ yr based on plasma parameters derived from X-ray data (Miyata et al. 1994) and $\sim 1.4 \times 10^4$ yr based on the shock model and X-ray measurements (Levenson et al. 1998).

Four LAT sources positionally associated with the Cygnus Loop SNR are listed in the 1FGL catalog (Abdo et al. 2010d). In this paper, we report a detailed analysis of *Fermi* LAT observations in the Cygnus Loop region. First, we briefly describe the observations and data selection in Section 2. The analysis procedure and the results are presented in Section 3, with the study of the morphology and spectrum of emission associated with the Cygnus Loop. Results are then discussed in Section 4 and our conclusions are presented in Section 5.

2. OBSERVATIONS AND DATA SELECTION

The LAT is the main instrument on *Fermi*, detecting gamma rays from ~ 20 MeV to > 300 GeV[1]. Details about the LAT instrument and pre-launch expectations for the performance can be found in Atwood et al. (2009). Compared to earlier high-energy

[1] As noted below in the present analysis we use only events with energies > 200 MeV.

gamma-ray telescopes, the LAT has a larger field of view (~ 2.4 sr), a larger effective area (~ 8000 cm^2 for >1 GeV on-axis) and improved point-spread function (PSF; the 68% containment angle > 1 GeV is smaller than 1°).

Routine science operations with the LAT began on August 4, 2008. We have analyzed events in the region of the Cygnus Loop collected from August 4, 2008, to August 1, 2010, with a total exposure of $\sim 6 \times 10^{10}$ cm^2 s (at 1 GeV). The LAT was operated in sky-survey mode for almost the entire period. In this observing mode the LAT scans the whole sky, obtaining complete sky coverage every 2 orbits (~ 3 hr) and approximately uniform exposure.

We used the standard LAT analysis software, the *ScienceTools* version v9r16, publicly available from the *Fermi* Science Support Center (FSSC)[2], and applied the following event selection criteria: 1) events have the highest probability of being gamma rays, i.e., they are classified in the so-called Pass 6 *Diffuse* class (Atwood et al. 2009), 2) events have a reconstructed zenith angle less than 105°, to minimize the contamination from Earth-limb gamma-ray emission, and 3) only time intervals when the center of the LAT field of view is within 52° of the local zenith are accepted to further reduce the contamination by Earth's atmospheric emission. We also eliminated two short periods of time during which the LAT detected the bright GeV-emitting GRB 081024B (Abdo et al. 2010c) and GRB 100116A (McEnery et al. 2010) within 15° of the Cygnus Loop. We restricted the analysis to the energy range > 200 MeV to avoid possible large systematics due to the rapidly varying effective area and much broader PSF at lower energies.

---

[2]Software and documentation of the *Fermi ScienceTools* are distributed by *Fermi* Science Support Center at http://fermi.gsfc.nasa.gov/ssc

3. ANALYSIS AND RESULTS

3.1. Morphological analysis

3.1.1. Method

In order to study the morphology of gamma-ray emission associated with the Cygnus Loop we performed a binned likelihood analysis based on Poisson statistics[3](see e.g. Mattox et al. 1996). We used only events above 0.5 GeV (compared to the 0.2 GeV used in the spectral analysis) for the morphological study to take advantage of the narrower PSF at higher energies. For this work we used the instrument response functions (IRFs) `P6_V3`, which were developed following the launch to address gamma-ray detection inefficiencies that are correlated with background rates (Rando et al. 2009). The analysis was performed over a square region of $12^\circ \times 12^\circ$ width with a pixel size of $0.^\circ 1$. We set the centroid of the region to (R.A., Dec.) = ($21^h 03^m 03^s$, $33^\circ 42' 56''$), 2° shifted from that of the Cygnus Loop toward negative Galactic latitudes to avoid the background given by Galactic diffuse emission and Galactic sources. Figure 1 (a) shows a count map in the 0.5–10 GeV energy band in the region used for the analysis, as well as the position of the Cygnus Loop from radio measurements and point sources in the 1FGL catalog. The four LAT sources, 1FGL J2046.4+3041, 1FGL J2049.1+3142, 1FGL J2055.2+3144 and 1FGL J2057.4+3057, are associated with the Cygnus Loop. Note that no gamma-ray pulsation was found for any of these LAT sources.

---

[3]As implemented in the publicly available *Fermi Science Tools*. The documentation concerning the analysis tools and the likelihood fitting procedure is available from http://fermi.gsfc.nasa.gov/ssc/data/analysis/documentation/Cicerone/.

3.1.2. Background model

Although the Cygnus Loop is at intermediate Galactic latitude, the contribution of the Galactic interstellar emission in the gamma-ray band is still important; it must be carefully modeled to perform morphological studies. Some of the interstellar gas tracers in the standard diffuse model provided by the LAT collaboration are not fully adequate for the Cygnus region, notably the E(B-V) map (Schlegel et al. 1998) because of infrared source contamination and temperature correction problems in such a massive-star forming region.

We therefore constructed a dedicated diffuse emission model. The model is analogous to the standard LAT diffuse model and it includes: a) an isotropic background, taking into account the isotropic diffuse gamma-ray emission as well as residual misclassified CR interactions in the LAT; b) large-scale Galactic inverse Compton emission produced by CR electrons and positrons upscattering low-energy photons, modeled using the GALPROP code (e.g. Porter et al. 2008); c) emission from interstellar gas arising from nucleon-nucleon interactions and electron Bremsstrahlung, which is modeled through spatial templates accounting for atomic gas and CO-bright molecular gas, partitioned along the line of sight to separate the Cygnus complex from the segments of the spiral arms in the outer Galaxy seen in this direction, as well as dark gas traced by visual extinction. With respect to the standard diffuse model, this one includes higher-resolution H I data (Taylor et al. 2003), visual extinction as a dark-gas tracer (Rowles & Froebrich 2009; Froebrich & Rowles 2010) and it is specifically tuned to reproduce LAT data in the Cygnus region, including the region of the Cygnus Loop. All these components, along with individual sources, were jointly fitted to the LAT data in 10 energy bands over the range 0.1–100 GeV with a free normalization in each energy bin (except for the inverse Compton model that was kept fixed). For further details we refer the reader to the dedicated paper (Ackermann et al. 2011), where the model is also discussed in detail in terms of CR and interstellar medium properties. We note that the presence of the Cygnus Loop was taken into account in this study. Several models were considered for the Loop, a combination of point sources and geometric templates such as a disk and a ring, as in the analysis performed in this paper. In this way we verified that the impact of the emission from the Cygnus Loop on the parameters of the global model of the region is small (Tibaldo 2011).

The results of this analysis were used to construct two model cubes, as a function of direction and energy, separately accounting for the isotropic and smooth large-scale Galactic inverse-Compton emission (a and b) and the structured emission from the gas (c). Such model cubes are part of the background model used to study the Cygnus Loop in this paper. For each of them we included a free normalization in order to further allow the model to adapt in the different cases we investigated along the paper.

In addition to interstellar emission, the background model to study the Cygnus Loop includes individual point-like sources in the 1FGL catalog within 15° of the Cygnus Loop except for the sources associated with the Cygnus Loop itself in the catalog; their positions were kept fixed at those given in the catalog and the spectra of the two gamma-ray pulsars in the region used for the analysis were modeled as power laws with exponential cutoffs leaving all spectral parameters free, while the spectra of the other sources were modeled as power laws leaving the integral fluxes as free parameters and assuming the spectral indices reported in the catalog. Note that, due to the PSF, which is poor compared to other wavelengths and strongly energy dependent, and the presence of a bright and structured background given by the interstellar emission, it is difficult to mask the background sources, and they are instead modeled along with the Cygnus Loop. The resulting model of background emission (i.e. not including emission associated with the Cygnus Loop) is shown in Figure 1 (b). The pulsars J2043+2740 and J2055+25 are the most important point sources in the vicinity, but the amount of events from those sources that fall within the Cygnus Loop (due to the broad low-energy PSF) is only 0.4 % and 0.2 % of the estimated emission from the Loop, respectively.

3.1.3. Comparison with observations at other wavelengths

Figure 2 shows the count map after subtracting the background emission in a $6^\circ \times 6^\circ$ region centered on the Cygnus Loop, (R.A., Dec.) = ($20^h51^m06^s$, $30^\circ41'00''$), with overlays of images at different wavelengths: X-rays, Hα line, radio continuum at 1420 MHz, infrared radiation at 100 μm and CO 2.6 mm line. The correlation between gamma rays, X-rays and Hα emission is evident. There is correlation among gamma rays and radio continuum emission in the northern part of the Cygnus Loop. On the other hand, the southern rim is brighter in radio continuum emission than in gamma rays, a phenomenon that perhaps might be explained by the existence of another SNR overlapping with the southern part of the Cygnus Loop (Uyanıker et al. 2002). The CO line intensities were integrated for velocities with respect to the local standard of rest -25 km s^{-1} $< V <$ 30 km s^{-1}[4]. No obvious association with CO emission is found; some molecular material is apparently located on the Western side of the Cygnus Loop, but the relationship is not clear. On the other hand, some correlation with thermal emission from dust at 100 μm, which can be considered as a proxy of total interstellar matter densities, is possible.

To quantitatively evaluate the correlation with emission at other wavebands, we fitted the LAT counts with the different models for the Cygnus Loop on top of the background model described above. First the Cygnus Loop was modeled with the four 1FGL sources, and then using the images at other wavelengths as spatial templates assuming a simple power-law spectrum. Note that we did not use the CO and infrared images as spatial

[4]The velocity corresponding to the distance from the Earth (540 pc) is ~ 0 km s^{-1}.

templates due to clear differences between them and the gamma-ray image as shown in Figure 2. The resulting maximum likelihood values with respect to the maximum likelihood for the null hypothesis (no emission associated with the Cygnus Loop) are summarized in Table 1. The test statistic (TS) values, i.e. $-2\ln(\text{likelihood ratio})$ (e.g. Mattox et al. 1996), for the X-ray and Hα images are significantly larger than for the four 1FGL sources. On the other hand, the TS for the radio image increases moderately in spite of the association in the northern rim, confirming that radio continuum structures in the southern rim do not well correlate with gamma-ray emission.

3.1.4. Geometrical Models

We further characterized the morphology of gamma-ray emission associated with the Loop by using simple parametrized geometrical models. We started with a uniform disk/ring assuming a simple power-law spectrum. We varied the radius and location of the disk and evaluated the maximum likelihood values. In the case of the ring, we varied inner and outer radii as well. The resulting TS values are reported in Table 1. The TS value for the ring with respect to the disk shape is $\simeq 12$. Assuming that, in the null hypothesis, the TS value is distributed as a χ^2 with n degrees of freedom, where n is the difference in degrees of freedom between the two nested models compared [5] ($n = 1$ in the present case), it would be equivalent to an improvement at $\sim$ 3.5 σ confidence level. Let us note, however, that the conversion of TS values into confidence level (or, equivalently, false positive rate) is subject to numerous caveats, see e.g. Protassov et al. (2002). We will thus take into account the source morphology uncertainties in the spectral analysis, below. In order to further illustrate the morphology of the gamma-ray emission, in Figure 3 we show its radial

[5]see link to *Fermi Science Tools* Cicerone

profile compared with the best-fit disk/ring models.

Finally, we want to verify if there are any spectral variations in the gamma-ray emission associated with the Cygnus Loop we are modeling as a whole. We thus divided the best-fit ring into four regions as shown in Figure 4 and allowed an independent normalization and spectral index for the four portions of the ring. There was no significant improvement of the likelihood for such a non-uniform ring. The TS value and power-law spectral index for each of the four regions of the remnant are reported for reference in Table 2. No significant differences are found between the four spectral indexes. Therefore we adopted the uniform ring template with maximum likelihood parameters for the whole SNR in the following spectral analysis.

3.2. Spectral analysis

To measure the spectrum we made maximum likelihood fits in 8 logarithmically-spaced energy bands from 0.2 GeV to 100 GeV, using the ring template as the model for the spatial distribution of the Cygnus Loop. Figure 5 shows the resulting spectral energy distribution (SED). Upper limits at the 90 % confidence level are calculated assuming a photon index of 2 if the detection is not significant in an energy bin, i.e., the TS value with respect to the null hypothesis is less than 10 (corresponding to 3.2 σ for one additional degree of freedom). Note that the value of the spectral index has a negligible effect on the upper limits.

We identify at least three different sources of systematic uncertainties affecting the estimate of the fluxes: uncertainties in the LAT event selection efficiency, the morphological template and the diffuse model adopted for analysis. Uncertainties in the LAT effective area are estimated to be 10 % at 100 MeV, decreasing to 5 % at 500 MeV, and increasing to 20 % at 10 GeV and above (Rando et al. 2009). Evaluating the systematic uncertainties due to the modeling of interstellar emission is a challenging task, because interstellar emission is highly structured and methods used at other wavelengths, like comparisons with neighboring regions, are not fully adequate in the GeV band. We therefore roughly gauged the related uncertainties by comparing the results with those obtained by adopting instead the standard LAT diffuse background models [6]. We similarly gauged the uncertainties due to the morphological template by comparing the results with those obtained by using the best-fit disk template instead of the ring. The total systematic errors are set by adding the above uncertainties in quadrature. Systematic uncertainties are driven by the imperfect knowledge of the background emission and, especially below a few hundred MeV, of the LAT response. In Figure 5 we show the uncertainties obtained following these prescriptions.

We probed for a spectral break in the LAT energy band by comparing the likelihood values of a spectral fit over the whole energy range considered based on a simple power law and other spectral functions. Note that no systematic uncertainties are accounted for in the likelihood fitting process. The TS values and best-fit parameters are summarized in Table 3. The fit with a log-parabola function yields a TS value of ~ 50 compared to a simple power-law model, which corresponds to an improvement at the $\sim 7\ \sigma$ confidence level. In spite of the uncertainties discussed above in the estimate of the confidence level, the large TS value is indicative of a significant improvement in the fit. A smoothly broken power law provides a very slight increase in the likelihood with respect to the log-parabola function, while a power law with exponential cutoff gives a worse fit. In conclusion, a simple power law as spectral model can be significantly rejected and from all the different models with cutoffs we get evidence for a steepening of the spectrum above 2–3 GeV. We detect gamma-ray emission with a formal significance of 23 σ for the above curved

[6] *gll_iem_v02* and *isotropic_iem_v02* available from the FSSC http://fermi.gsfc.nasa.gov/ssc/data/access/lat/BackgroundModels.html

spectral shapes. The observed photon flux and energy flux in the 0.2–100 GeV range are $5.0^{+0.6}_{-0.6} \times 10^{-8}$ cm^{-2} s^{-1} and $6.5^{+0.7}_{-0.6} \times 10^{-11}$ erg cm^{-2} s^{-1}, respectively.

4. DISCUSSION

The gamma-ray luminosity inferred from our analysis is $\sim 1 \times 10^{33}$erg s^{-1} between 1–100 GeV, lower by one order of magnitude than observed for other GeV-emitting SNRs (typically $> 10^{34}$ erg s^{-1}, Abdo et al. 2009, 2010a,b,e,f). The spatial distribution is best represented by a ring with inner/outer radii $0^{\circ}.7 \pm 0^{\circ}.1$ and $1^{\circ}.6 \pm 0^{\circ}.1$, respectively. This makes the Cygnus Loop the largest gamma-ray emitting SNR observed so far, allowing us to perform a detailed morphological comparison with emission at other wavelengths.

There is a correspondence among gamma-ray emission, X-ray rims and Hα filaments, indicating that the high-energy particles responsible for gamma-ray emission are in the vicinity of the shock regions. The Balmer-dominated filaments define the current location of the blast wave and mark the presence of neutral material. Detailed studies of the particular locations at the northeast have used these nonradiative shocks as density probes (Raymond et al. 1983; Long et al. 1992; Hester et al. 1994) and derived post-shock densities of ~ 5 cm^{-3} where gamma-ray emission is expected to be bright due to the compressed material and high density of accelerated particles.

The radio continuum emission, originated by high-energy electrons via synchrotron radiation, is well correlated with gamma-ray emission in the northern region of the remnant but not in the southern one The presence of a second SNR was suggested by Uyanıker et al. (2002). The two SNRs would be at about the same distance based on the rotation measure analysis of the radio data (Sun et al. 2006). The lack of correlation between gamma rays and radio continuum emission in the southern region plausibly implies that the second SNR is not producing significant gamma-ray emission at our current sensitivity. There might be some correlation between total matter densities as traced by infrared thermal emission from dust and gamma-ray emission, whereas CO emission does not obviously overlap with the Cygnus Loop.

From these considerations, we argue that the bulk of gamma-ray emission comes from interactions of high-energy particles accelerated at the shocks of the Cygnus Loop with interstellar matter or fields in the regions just adjacent to the shocks with a gas density of ~ 5 cm $^{-3}$.

To model the broadband emission from the entire SNR we adopt the simplest possible assumption that gamma rays are emitted by a population of accelerated protons and electrons distributed in the same region and characterized by constant matter density and magnetic field strength. We assume the injected electrons to have the same momentum distribution as protons. This assumption requires a break in the momentum spectrum because the spectral index in the radio domain, corresponding to lower particle momenta, is much harder than for gamma rays, which correspond to higher particle momenta. Therefore, we use the following functional form to model the momentum distribution of injected particles:

$$Q_{e,p}(p) = a_{e,p} \left(\frac{p}{1 \text{ GeV } c^{-1}} \right)^{-s_{\rm L}} \left\{ 1 + \left(\frac{p}{p_{\rm br}} \right)^2 \right\}^{-(s_{\rm H}-s_{\rm L})/2}, \tag{1}$$

where $p_{\rm br}$ is the break momentum, $s_{\rm L}$ is the spectral index below the break and $s_{\rm H}$ above the break. Note that here we consider minimum momenta of 100 MeV c^{-1} since the details of the proton/electron injection process are poorly known.

Electrons suffer energy losses due to ionization, Coulomb scattering, Bremsstrahlung, synchrotron emission and inverse Compton (IC) scattering. We calculated the evolution of the electron momenta spectrum by the following equation:

$$\frac{\partial N_{e,p}}{\partial t} = \frac{\partial}{\partial p} \left(b_{e,p} N_{e,p} \right) + Q_{e,p}, \tag{2}$$

where $b_{e,p} = -dp/dt$ is the momentum loss rate, and $Q_{e,p}$ is the particle injection rate. We assume $Q_{e,p}$ to be constant, i.e., that the shock produces a constant number of particles until the SNR enters the radiative phase, at which time the source turns off. This prescription approximates the weakening of the shock and the reduction in the particle acceleration efficiency, which would be properly treated by using a time-dependent shock compression ratio (Moraal & Axford 1983). To derive the remnant emission spectrum we calculated $N_{e,p}(p, T_0)$ numerically, where T_0 is the SNR age of 2×10^4 yr. Note that we neglected the momentum losses for protons since the timescale of neutral pion production is $\sim 10^7/\bar{n}_{\rm H}$ yr where $\bar{n}_{\rm H}$ is the gas density averaged over the entire SNR shell and is much longer than the SNR age. Also we do not consider the gamma-ray emission by secondary positrons and electrons from charged pion decay, because the emission from secondaries is generally unimportant relative to that from primary electrons unless the gas density is as high as that in dense molecular clouds and the SNR evolution reaches the later stages, or the injected electron-to-proton ratio is much lower than locally observed. The gamma-ray spectrum from π^0 decay produced by the interactions of protons with ambient hydrogen is calculated based on Dermer (1986) using a scaling factor of 1.84 to account for helium and heavier nuclei in target material and cosmic rays (Mori 2009). Contributions from bremsstrahlung and inverse Compton scattering by accelerated electrons are computed based on Blumenthal & Gould (1970), whereas synchrotron radiation is based on Crusius & Schlickeiser (1986).

First, we consider a π^0-decay dominated model. The number index of protons in the high-energy regime is constrained to be $s_{\rm H} \approx 2.6$ from the gamma-ray spectral slope. The spectral index of the proton momentum below the break is determined to be $s_{\rm L} \approx 1.8$ by modeling the radio spectrum as synchrotron radiation by relativistic electrons (under the assumption that protons and electrons have identical injection spectra). The spectral index α of the radio continuum emission is ~ 0.4 (Uyanıker et al. 2004), where α is defined as $S_\nu \propto \nu^{-\alpha}$ with S_ν and ν the flux density and the frequency, respectively. It is difficult to derive the break momentum of the proton spectrum from the gamma-ray spectrum, since in the GeV energy band we expect a curvature due to kinematics of π^0 production and decay. The gamma-ray spectrum provides thus only an upper bound for the momentum break at ~ 10 GeV c^{-1}. On the other hand, the momentum break cannot be lower than ~ 1 GeV c^{-1} to avoid conflicts with radio data. We adopt a break at the best-fit value, 2 GeV c^{-1}. The resulting total proton energy, $W_p \sim 2.6 \times 10^{48} \cdot (5\ \mathrm{cm}^{-3}/\bar{n}_\mathrm{H}) \cdot (d/540\ \mathrm{pc})^2$ erg, is less than 1 % of the typical kinetic energy of a supernova explosion. For an electron-to-proton ratio $K_{ep} = 0.01$ at 1 GeV c^{-1}, which is the ratio measured at the Earth, the magnetic field strength is constrained to be $B \sim 60$ μG by radio data. The magnetic field strength of the undisturbed medium in the northeastern rim was estimated to be ~ 20 μG by van der Laan (1962) based on the measurements of shell thickness and expansion velocities together with the theory of hydromagnetic shock propagation given the density of the undisturbed medium $\sim 1\ \mathrm{cm}^{-3}$ (e.g., Hester et al. 1994). The compression behind the shock front indicates a magnetic field strength similar to the value used above in the modeling. Using the parameters summarized in Table 4, we obtained the SEDs shown in Figure 6 (a).

It is difficult to model the gamma-ray spectrum with a model dominated by electron bremsstrahlung because the break in the electron spectrum required to reproduce the gamma-ray spectrum would appear in the radio domain as shown in Figure 6 (b).

The gamma-ray spectrum can be reproduced by an inverse Compton dominated model shown in Figure6 (c). Gamma-ray emission of IC origin is due to interactions of high-energy electrons with optical and infrared radiation fields and the cosmic microwave background (CMB). We used in our calculations the first two components as they are modeled in Porter et al. (2008) at the location of the Cygnus Loop. Since their spectra are very complex, they are approximated by two infrared and two optical blackbody components. The flux ratio between the IC and the synchrotron components constrains the magnetic field to be less than 2 μG and requires a low gas density of $\bar{n}_{\rm H} \sim 2 \times 10^{-2}$ cm^{-3} to suppress the electron bremsstrahlung. Although such a low density may exist inside the remnant based on X-ray observations (e.g., Ku et al. 1984), gamma-ray emission peaks at the shock regions where the gas density is $\sim 1 - 5$ cm $^{-3}$ (see above). Increasing the intensity of the interstellar radiation field would loosen the constraint on the gas density. However, a radiation field about 50 times more intense is required to satisfy the above assumption on the gas density.

To summarize, it is most natural to assume that gamma-ray emission from the Cygnus Loop is dominated by decay of π^0 produced in nucleon-nucleon interactions of hadronic cosmic rays with interstellar matter. It should be emphasized that our observations of the Cygnus Loop combined with the radio data constrain the proton momentum break to be in the range, 1–10 GeV c^{-1}, despite the lack of association with dense molecular clouds unlike the other middle-aged SNRs detected with the LAT. Thus in this case cosmic rays responsible for gamma-ray emission are localized near their acceleration sites without significant diffusion taking place. The correspondence observed between gamma rays and Hα emission may be accounted for in the "crushed cloud" scenario by Uchiyama et al. (2010), although the expected filaments cannot be resolved by current gamma-ray telescopes. The predictions by Inoue et al. (2010) cannot be directly compared to the Cygnus Loop since their simulations were performed for environments characterized by dense clouds. However, the scenario of acceleration by reflected shocks might be operative, on consideration of X-ray and optical observations (e.g., Graham et al. 1995).

5. CONCLUSIONS

We analyzed gamma-ray measurements by the LAT in the region of the Cygnus Loop, detecting significant gamma-ray emission associated with the remnant. The gamma-ray luminosity is $\sim 1 \times 10^{33}$erg s^{-1} between 1–100 GeV, lower than for other GeV-emitting SNRs studied with LAT data. The morphology of gamma-ray emission is best represented by a ring with inner/outer radii $0.^{\circ}7 \pm 0^{\circ}.1$ and $1.^{\circ}6 \pm 0^{\circ}.1$. The Cygnus Loop is thus the most extended gamma-ray emitting SNR detected in the GeV band so far and the morphology of gamma-ray emission can be compared in detail with observations at other wavelengths. There is correspondence among gamma rays, the X-ray rims and the Hα filaments, indicating that the high-energy particles responsible for the gamma-ray emission are in the vicinity of the shock regions.

The gamma-ray spectrum has a break in the 2–3 GeV energy range. The decay of π^0 produced by interactions of hadrons accelerated by the remnant with interstellar gas naturally explains the gamma-ray spectrum. In this scenario our observations of the Cygnus Loop indicate that the proton momentum spectrum is steep in the high-energy regime, with a spectral break which is constrained together with radio continuum emission in the range 1–10 GeV c^{-1}. The absence of molecular clouds in the areas of gamma-ray emission (contrary to other middle-aged Fermi SNRs) constrains some of the scenarios invoked to explain the observed spectral properties of GeV emitting SNRs.

The *Fermi* LAT Collaboration acknowledges generous ongoing support from a number of agencies and institutes that have supported both the development and the operation of the LAT as well as scientific data analysis. These include the National Aeronautics and Space Administration and the Department of Energy in the United States, the Commissariat à l'Energie Atomique and the Centre National de la Recherche Scientifique

/ Institut National de Physique Nucléaire et de Physique des Particules in France, the Agenzia Spaziale Italiana and the Istituto Nazionale di Fisica Nucleare in Italy, the Ministry of Education, Culture, Sports, Science and Technology (MEXT), High Energy Accelerator Research Organization (KEK) and Japan Aerospace Exploration Agency (JAXA) in Japan, and the K. A. Wallenberg Foundation, the Swedish Research Council and the Swedish National Space Board in Sweden.

Additional support for science analysis during the operations phase is gratefully acknowledged from the Istituto Nazionale di Astrofisica in Italy and the Centre National d'Études Spatiales in France.

We have made use of the *ROSAT* Data Archive of the Max-Planck-Institut für extraterrestrische Physik (MPE) at Garching, Germany. The Digitized Sky Surveys were produced at the Space Telescope Science Institute under U.S. Government grant NAG W-2166. The images of these surveys are based on photographic data obtained using the Oschin Schmidt Telescope on Palomar Mountain and the UK Schmidt Telescope. The plates were processed into the present compressed digital form with the permission of these institutions.

REFERENCES

Abdo, A. A., et al. (The *Fermi* LAT Collaboration) 2009, ApJ, 706, L1

Abdo, A. A., et al. (The *Fermi* LAT Collaboration) 2010, Science, 327, 1103

Abdo, A. A., et al. (The *Fermi* LAT Collaboration) 2010, ApJ, 712, 459

Abdo, A. A., et al. (The *Fermi* LAT Collaboration) 2010, ApJ, 712, 558

Abdo, A. A., et al. (The *Fermi* LAT Collaboration) 2010, ApJS, 188, 405

Abdo, A. A., et al. (The *Fermi* LAT Collaboration) 2010, ApJ, 718, 348

Abdo, A. A., et al. (The *Fermi* LAT Collaboration) 2010, ApJ, 722, 1303

Ackermann, M., et al. (The *Fermi* LAT Collaboration) 2011, submitted

Aharonian, F. A., & Atoyan, A. M. 1996, A&A, 309, 917

Atwood, W. B., et al. (The *Fermi* LAT Collaboration) 2009, ApJ, 697, 1071

Beichman, C. A., Neugebauer, G., Habing, H. J., Clegg, P. E., & Chester, T. J. 1988, Infrared astronomical satellite (IRAS) catalogs and atlases. Volume 1: Explanatory supplement, 1,

Blair, W. P., Sankrit, R., & Raymond, J. C. 2005, AJ, 129, 2268

Blandford, R. D. & Eichler, D. 1987, Phys. Rep., 154, 1

Blumenthal, G. R., & Gould, R. J. 1970, Reviews of Modern Physics, 42, 237

Crusius, A., & Schlickeiser, R. 1986, A&A, 164, L16

Dame, T. M. 2011, arXiv:1101.1499

Dame, T. M., Hartmann, D., & Thaddeus, P. 2001, ApJ, 547, 792

de Noyer, L. K. 1975, ApJ, 196, 479

Dermer, C. D. 1986, A&A, 157, 223

Froebrich, D., & Rowles, J. 2010, MNRAS, 406, 1350

Gabici, S., Aharonian, F. A., & Casanova, S. 2009, MNRAS, 396, 1629

Graham, J. R., Levenson, N. A., Hester, J. J., Raymond, J. C., & Petre, R. 1995, ApJ, 444, 787

Hester, J. J., Raymond, J. C., & Blair, W. P. 1994, ApJ, 420, 721

Inoue, T., Yamazaki, R., & Inutsuka, S.-i. 2010, ApJ, 723, L108

Keen, N. J., Wilson, W. E., Haslam, C. G. T., Graham, D. A., & Thomasson, P. 1973, A&A, 28, 197

Ku, W. H.-M., Kahn, S. M., Pisarski, R., & Long, K. S. 1984, ApJ, 278, 615

Levenson, N. A., Graham, J. R., Keller, L. D., & Richter, M. J. 1998, ApJS, 118, 541

Long, K. S., Blair, W. P., Vancura, O., Bowers, C. W., Davidsen, A. F., & Raymond, J. C. 1992, ApJ, 400, 214

Mattox, J. R., et al. , 1996, ApJ, 461, 396

McEnery, J., Chiang, J., Omodei, N., & Nakamori, T. 2010, GRB Coordinates Network, Circular Service, 10333, 1 (2010), 333, 1

Miyata, E., Tsunemi, H., Pisarski, R., & Kissel, S. E. 1994, PASJ, 46, L101

Moraal, H., & Axford, W. I. 1983, A&A, 125, 204

Mori, M., 2009, Astropart. Phys., 31, 341

Ohira, Y., Murase, K., & Yamazaki, R. 2011, MNRAS, 410, 1577

Porter, T., et al. 2008, ApJ, 682, 400

Protassov, R., van Dyk, D. A., Connors, A., Kashyap, V. L., & Siemiginowska, A. 2002, ApJ, 571, 545

Rando, R. et al., arXiv:0907.0626

Raymond, J. C., Blair, W. P., Fesen, R. A., & Gull, T. R. 1983, ApJ, 275, 636

Reich, W. 1982, A&AS, 48, 219

Rowles, J., & Froebrich, D. 2009, MNRAS, 395, 1640

Schlegel, D. J., Finkbeiner, D. P., & Davis, M. 1998, ApJ, 500, 525

Scoville, N. Z., Irvine, W. M., Wannier, P. G., & Predmore, C. R. 1977, ApJ, 216, 320

Sun, X. H., Reich, W., Han, J. L., Reich, P., & Wielebinski, R. 2006, A&A, 447, 937

Taylor, A. R., Gibson, S. J., Peracaula, M., et al. 2003, AJ, 125, 3145

Tibaldo, L. 2011, PhD thesis, Universities of Padova and Paris Diderot

Torres, D. F., Marrero, A. Y. R., & de Cea Del Pozo, E. 2010, MNRAS, 408, 1257

Uchiyama, Y., Blandford, R. D., Funk, S., Tajima, H., & Tanaka, T. 2010, ApJ, 723, L122

Uyanıker, B., Reich, W., Yar, A., Kothes, R., Fürst, E. 2002, A&A, 389, L61

Uyanıker, B., Reich, W., Yar, A., Fürst, E. 2004, A&A, 426, 909

van der Laan, H. 1962, MNRAS, 124, 125

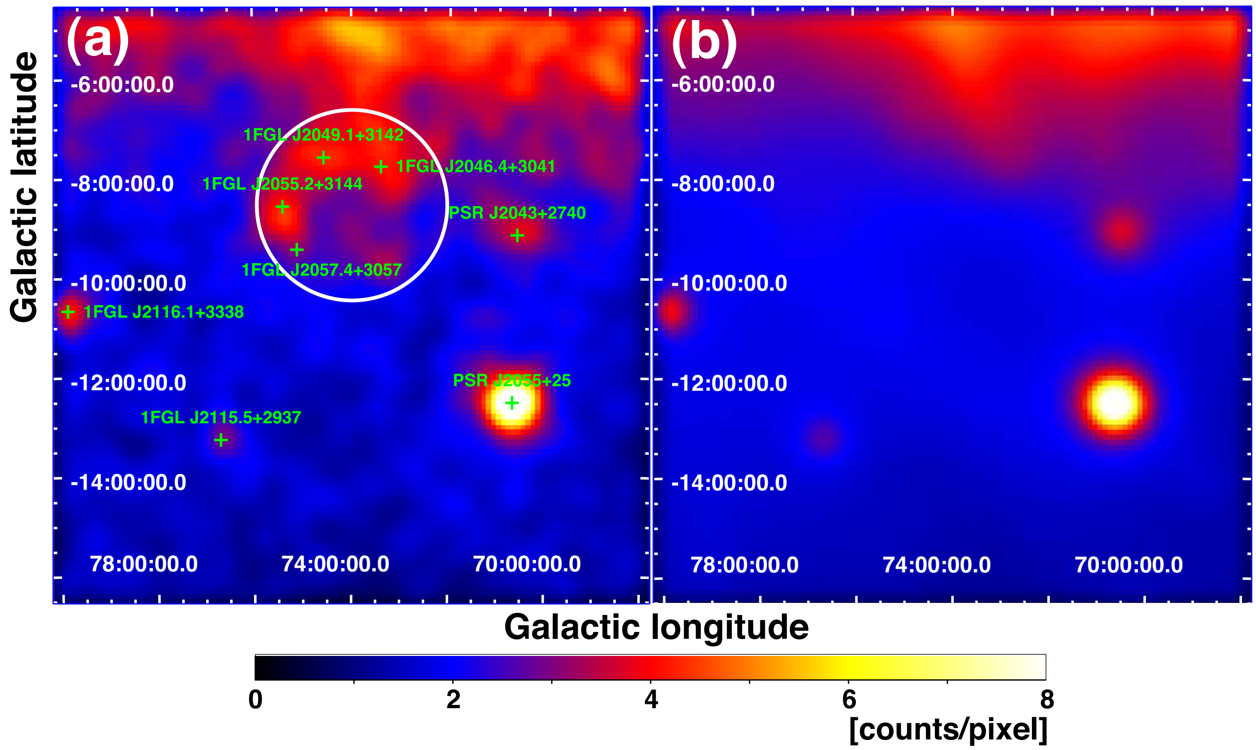

Fig. 1.— (a) *Fermi* LAT count map in the Cygnus Loop region for photon energies 0.5–10 GeV. The count map has a pixel size of 0.°1 and is smoothed for display with a Gaussian kernel of $\sigma = 0.°5$. Note that all along the paper the analysis is conducted on unsmoothed data taking into account the instrument PSF in the likelihood analysis. The white circle is the location of the Cygnus Loop, defined by its radio emission. Green crosses indicate the positions of gamma-ray sources listed in the 1FGL catalog (Abdo et al. 2010d). (b) count map expected from the background model (taking into account the LAT PSF). The four LAT point sources associated with the Cygnus Loop are not included in the model. The image is binned and smoothed in the same manner as the real data.

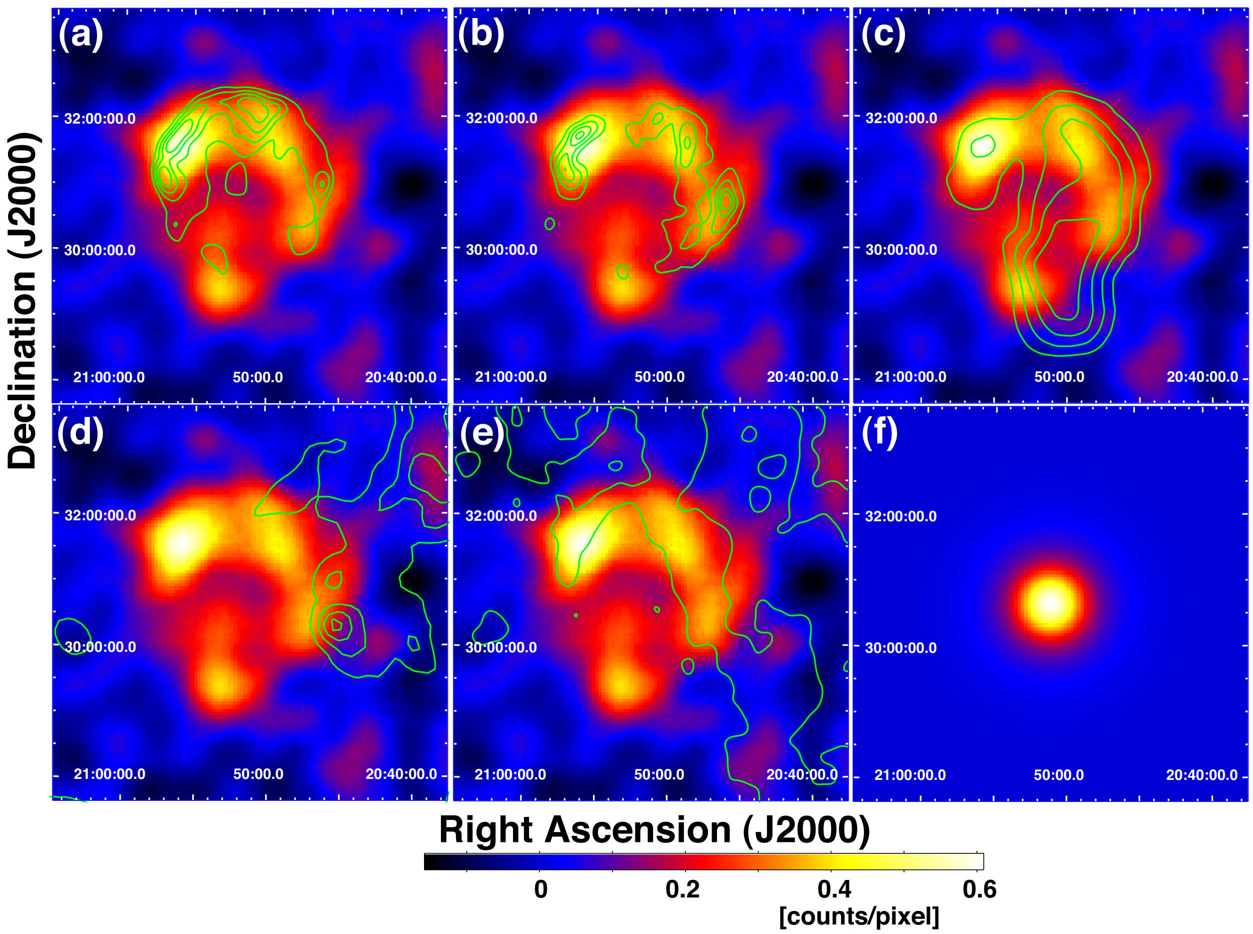

Fig. 2.— Background-subtracted LAT count map in the 0.5–10 GeV energy range. The count map is binned using a grid of 0.°05 and smoothed with a Gaussian kernel of $\sigma = 0.°5$. Negative residuals are shown to gauge the quality of the subtraction of the background emission. Green contours correspond to images at different wavelengths. (a) X-ray count map (0.1–2 keV) by *ROSAT*. Contours are at 20, 40, 60, 80 % levels; the image was first cleaned from background emission, estimated by fitting data surrounding the Cygnus Loop with a bilinear function, and smoothed with a Gaussian kernel of $\sigma = 0.°2$; (b) Hα image obtained from the publicly available Digital Sky Survey obtained with the same procedure explained for X-ray data. We selected the POSS-II F (red) filtered survey whose transmission coefficient peaked near Hα . (c) 1420 MHz radio continuum emission (Reich 1982); extraction of the contours as for the previous images. (d) ^{12}CO ($J = 1 \rightarrow 0$) line intensities integrated for velocities from -25 km s^{-1} to 30 km s $^{-1}$. The data are taken from the CfA survey (Dame et al. 2001) cleaned from background using the moment-masking technique (Dame 2011); the image was smoothed using a Gaussian kernel with $\sigma = 0.°25$; contours are at 1, 4, 7, 10 K km s^{-1}. (e) The infrared intensity map at 100 μm by InfraRed Astronomical Satellite (IRAS) (Beichman et al. 1988); the image was smoothed using a Gaussian kernel of $\sigma = 0.°2$; contours are at 15, 25, 35, 45 MJy sr^{-1}. The contour at the top-right corner is the highest one. (f) the effective LAT PSF in the energy band of the LAT count map for a photon spectral index of 2.5. The PSF map is binned and smoothed in the same manner as the real data.

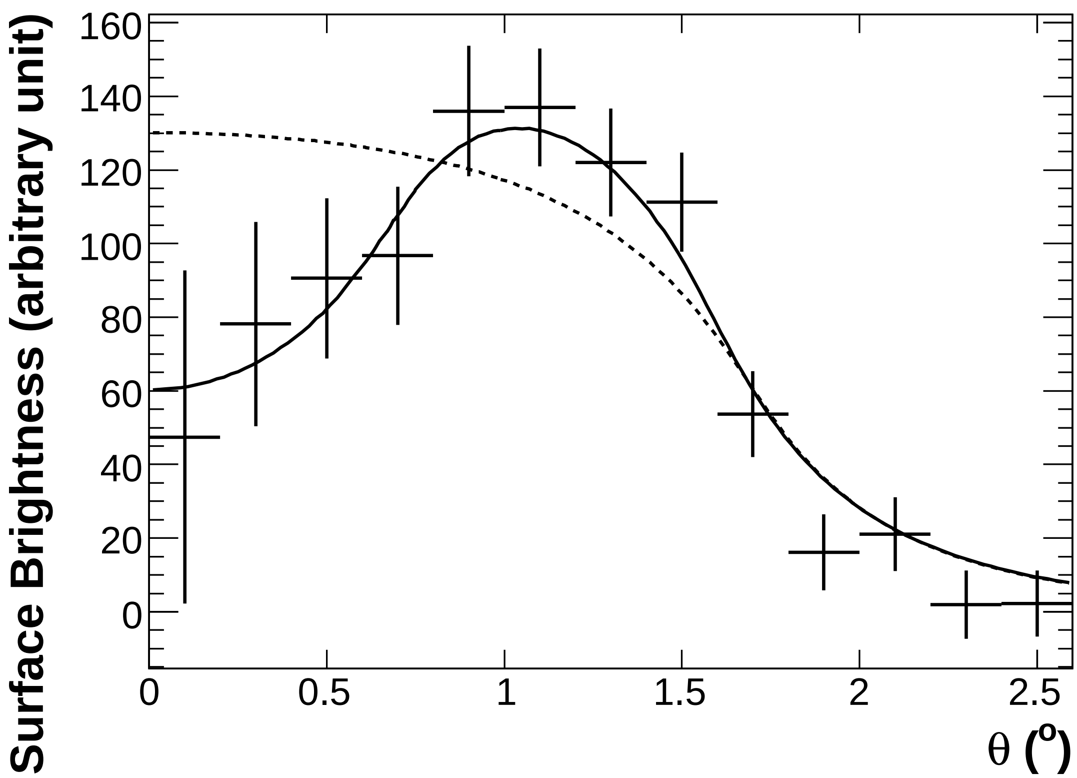

Fig. 3.— Radial profile of the Cygnus Loop in gamma rays in the 0.5–10 GeV energy range (crosses). The origin is the center of the best-fit ring model. Gamma-ray data have the background emission subtracted. Note that the data are not smoothed. Overlaid are the distributions expected for the best-fit ring shape (solid line) and the best-fit disk shape (dotted line) as emission surfaces, with parameters fit to gamma-ray data taking the LAT instrument response into account. Details of the fits are described in the text.

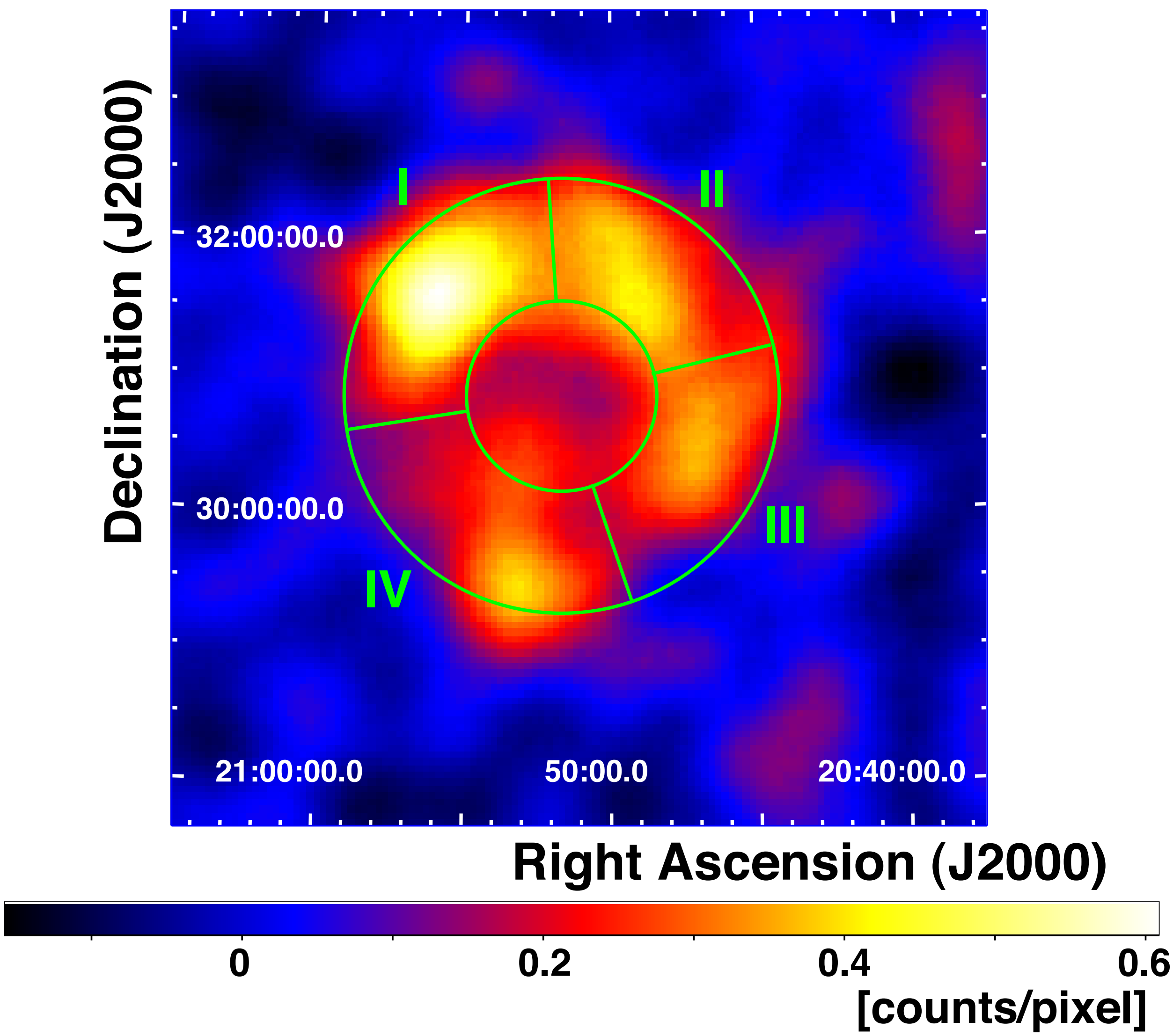

Fig. 4.— Definitions of the regions of the Cygnus Loop used for the morphology analysis (§ 3.1) overlaid on the LAT count map as shown in Figure 2.

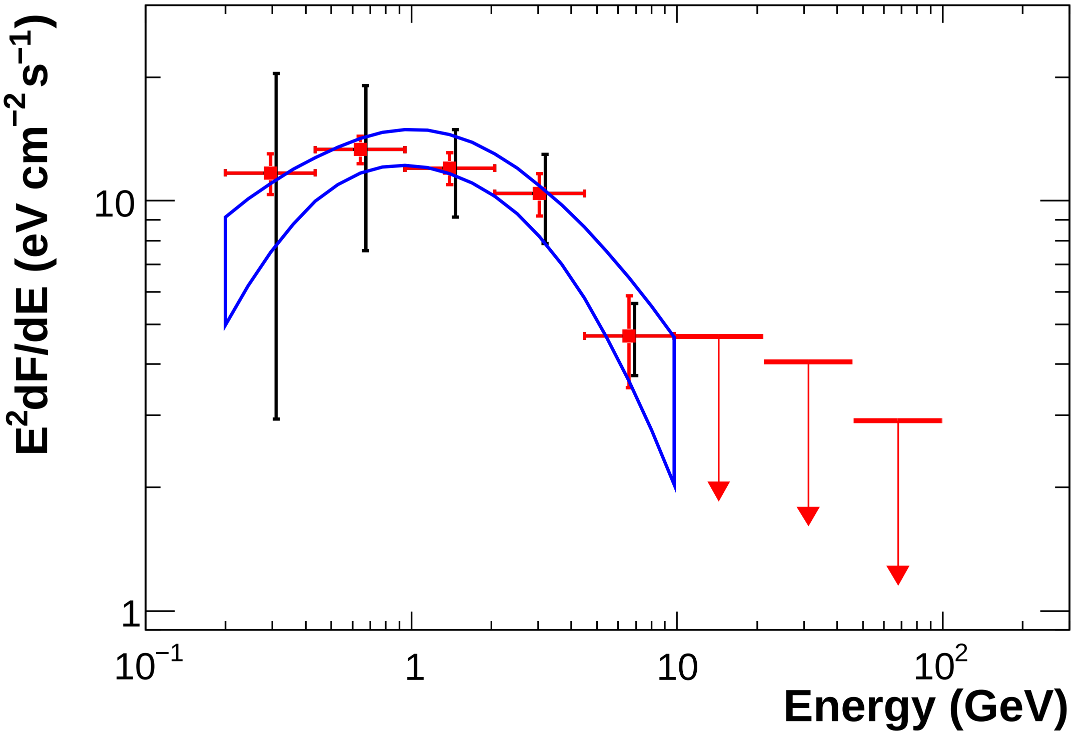

Fig. 5.— Spectral energy distribution of the gamma-ray emission measured by the LAT for the Cygnus Loop. Red squares are LAT flux points. Horizontal bars indicate the energy range the flux refers to. Vertical bars show statistical errors in red and systematic errors (added in quadrature for illustration purposes) in black. In energy bins where the detection is not significant (test statistic < 10) we show upper limits at the 90 % confidence level. The blue region is the 68 % confidence range (no systematic error) of the LAT spectrum assuming that the spectral shape is a log parabola.

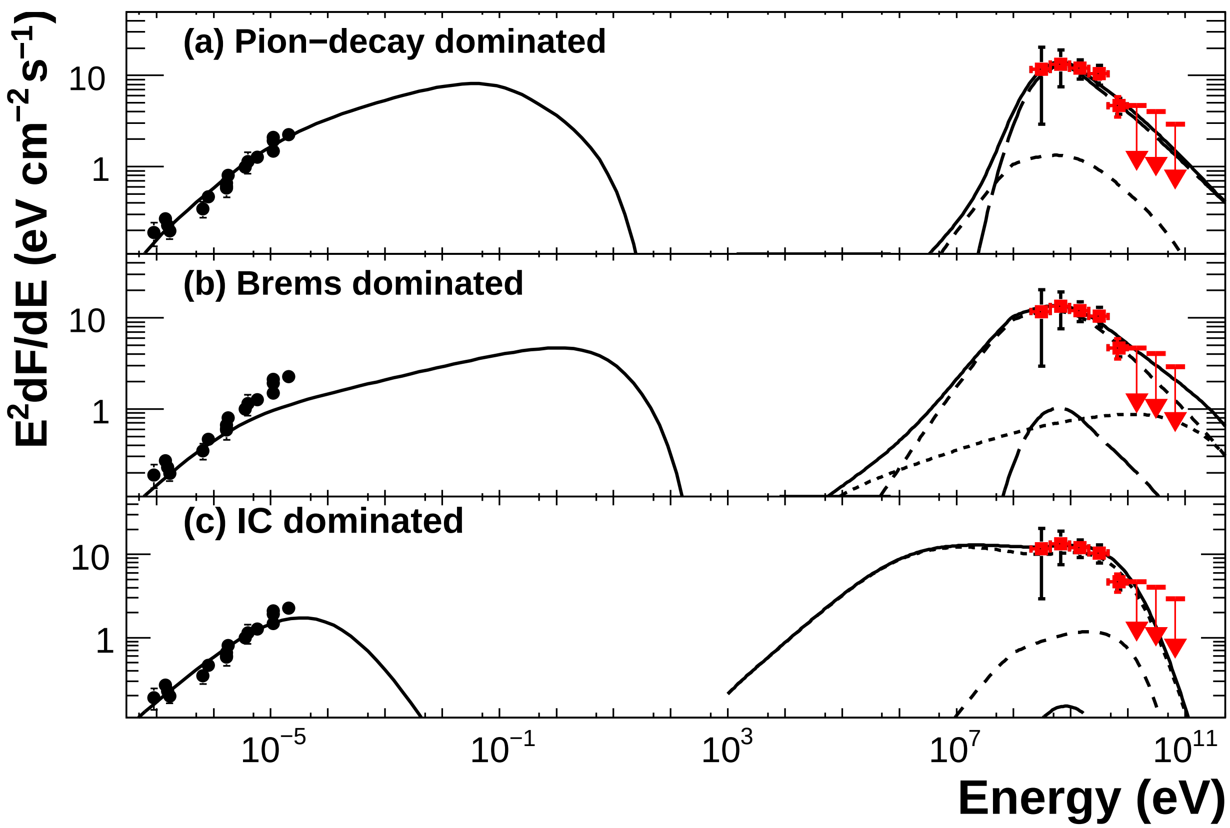

Fig. 6.— Multi-band spectrum of the Cygnus Loop. In the GeV band LAT measurements are reported as in Figure 5. The radio continuum emission (Uyanıker et al. 2004) is shown by black dots. Radio emission is modeled as synchrotron radiation, while gamma-ray emission is modeled by different combinations of π^0-decay (long-dashed curve), bremsstrahlung (dashed curve), and inverse Compton (IC) scattering (dotted curve). Details of the models are described in the text: a) π^0-decay dominated model, b) bremsstrahlung dominated model, c) IC dominated model.

Table 1: Test Statistics for Different Spatial Models Compared with the Null Hypothesis of No Gamma-ray Emission Associated with the Cygnus Loop (0.5–100 GeV)

Model	Test Statistic[a]	Additional Degrees of Freedom
Null hypothesis[b]	0	0
4 point sources[c]	318	8
ROSAT X-rays (0.1–2keV)[d]	406	2
Hα [d]	434	2
1420MHz radio continuum[d]	343	2
Uniform disk[e]	441	5
Uniform ring[f]	453	6
Non-uniform ring[g]	464	12

[a] $-2\ln(L_0/L)$, where L and L_0 are the maximum likelihoods for the model with/without the source component, respectively.

[b] Background only (no model for the Cygnus Loop).

[c] The four sources listed in the 1FGL source list associated with the Cygnus Loop (Abdo et al. 2010d).

[d] Background-subtracted as described in Figure 2.

[e] The best fit parameters are: radius $1^\circ.7 \pm 0^\circ.1$ and centroid (R.A., Dec.) = (20^h52^m, $30^\circ50'$). The error of the centroid is $0^\circ.04$ at 68 % confidence level.

[f] The best fit parameters are: inner/outer radii $0^\circ.7 \pm 0^\circ.1$, and $1^\circ.6 \pm 0^\circ.1$, centroid (R.A., Dec.) = (20^h51^m, $30^\circ50'$). The error of the centroid is $0^\circ.04$ at 68 % confidence level.

[g] The best-fit ring were divided into four regions as shown in Figure 4 and allowed an independent normalization and spectral index for the four portions of the ring.

Table 2: Test Statistics and Power-law Spectral Indexes for the Four Regions of the Remnant as Defined in Figure 4 (0.5–100 GeV)

Region	Test Statistic[a]	Spectral Index
I	143	2.49 ± 0.10
II	73	2.32 ± 0.12
III	64	2.25 ± 0.15
IV	41	2.37 ± 0.14

[a] $-2\ln(L_0/L)$, where L and L_0 are the maximum likelihoods for the model with/without the source component, respectively.

Table 3: Test Statistics and Parameters for Various Spectral Models (0.2–100 GeV)

Spectral Model	Test Statistic[a]	Degrees of Freedom	Spectral Parameters
Power law	0	2	E^{-p}; $p = 2.23 \pm 0.02$
Power law with exponential cutoff	42	3	$E^{-p} \exp\left(-\frac{E}{E_\mathrm{b}}\right)$; $p = 1.57 \pm 0.12$ $E_\mathrm{b} = 3.02 \pm 0.65$ GeV
Log Parabola	50	3	$\left(\frac{E}{1\ \mathrm{GeV}}\right)^{-p_1 - p_2 \log\left(\frac{E}{1\ \mathrm{GeV}}\right)}$ $p_1 = 2.02 \pm 0.03$ $p_2 = 0.27 \pm 0.02$
Smoothly broken power law	51	4	$E^{-p_1} \left\{1 + \left(\frac{E}{E_\mathrm{b}}\right)^{\frac{-p1+p2}{0.2}}\right\}^{-0.2}$ $p_1 = 1.83 \pm 0.06$ $p_2 = 3.23 \pm 0.19$ $E_\mathrm{b} = 2.39 \pm 0.26$ GeV

[a] $-2\ln(L_0/L)$, where L and L_0 are the maximum likelihood values for the model under consideration and the power-law model, respectively.

Note. — The test statistics for the best-fit uniform ring with exponential cutoff, log parabola, and smoothly broken power law with respect to the null hypothesis of no emission associated with the Cygnus Loop are 572, 580, and 581 in the energy band 0.2–100 GeV.

Table 4: Model parameters for the Cygnus Loop.

Model	K_{ep}[a]	s_{L}[b]	p_{br}[c] (GeV c^{-1})	s_{H}[d]	B (μG)	$\bar{n}_{\mathrm{H}}$[e] (cm^{-3})	W_p[f] (10^{48} erg)	W_e[f] (10^{48} erg)
(a) Pion	0.01	1.8	2	2.6	60	5	2.6	4.9×10^{-2}
(b) Bremsstrahlung	1	1.8	2	2.7	12	5	0.21	0.43
(c) Inverse Compton[g]	1	1.8	25	5.0	1.8	0.02	5.9	9.8

[a]The ratio electrons-to-protons at 1 GeV c^{-1}.

[b]The momentum distribution of particles is assumed to be a smoothly broken power-law, where the indices and the break momentum are identical for both accelerated protons and electrons. s_{L} is the spectral index in momentum below the break.

[c]p_{br} is the break momentum.

[d]Spectral index in momentum above the break.

[e]Average hydrogen number density of ambient medium.

[f]The distance from the Earth is assumed to be 540 pc (Blair et al. 2005). The total energy is calculated for particles > 100 MeV c^{-1}.

[g]Seed photons for inverse Compton scattering of electrons include the CMB, two infrared ($T_{\mathrm{IR}} = 34, 4.7 \times 10^2$ K, $U_{\mathrm{IR}} = 0.34, 6.3 \times 10^{-2}$ eV cm^{-3}, respectively), and two optical components ($T_{\mathrm{opt}} = 3.6 \times 10^3, 9.9 \times 10^3$ K, $U_{\mathrm{opt}} = 0.45, 0.16$ eV cm^{-3}, respectively) in the vicinity of the Cygnus Loop.